

Decoupling Torque and Stiffness: A Unified Modeling and Control Framework for Antagonistic Artificial Muscles

Amirhossein Kazemipour¹ and Robert K. Katzschmann¹

Abstract—Antagonistic soft actuators built from artificial muscles (PAMs, HASELs, DEAs) promise plant-level torque-stiffness decoupling, yet existing controllers for soft muscles struggle to maintain independent control through dynamic contact transients. We present a unified framework enabling independent torque and stiffness commands in real-time for diverse soft actuator types. Our unified force law captures diverse soft muscle physics in a single model with sub-ms computation, while our cascaded controller with analytical inverse dynamics maintains decoupling despite model errors and disturbances. Using co-contraction/bias coordinates, the controller independently modulates torque via bias and stiffness via co-contraction—replicating biological impedance strategies. Simulation-based validation through contact experiments demonstrates maintained independence: 200× faster settling on soft surfaces, 81% force reduction on rigid surfaces, and stable interaction vs 22–54% stability for fixed policies. This framework provides a foundation for enabling musculoskeletal antagonistic systems to execute adaptive impedance control for safe human-robot interaction.

Index Terms—Antagonistic Actuation, Artificial Muscles, Variable Impedance Control, Dynamic Modeling, System Identification.

I. INTRODUCTION

Biological motor systems demonstrate a remarkable principle: they decouple force production from mechanical stiffness through antagonistic muscle arrangements [1]. During rapid movements and unexpected contacts, muscle stiffness can modulate in tens of milliseconds (faster than voluntary neural commands can contribute) through intrinsic muscle properties and spinal reflexes [2], [3]. This mechanical intelligence, encoded in the properties of muscle and tendon rather than in computation, enables robust interaction with unpredictable environments without explicit sensing or classification [4].

Artificial muscles, including pneumatic (PAMs/McKibben), electrohydraulic (HASELs), and dielectric elastomer actuators (DEAs), promise to bring this biological capability to robotics [5], [6], [7]. These soft actuators offer inherent compliance and high power-to-weight ratios, making them attractive for musculoskeletal robots that aim to replicate animal-like agility [8], [9], [10]. However, despite their diverse operating principles, they share fundamental force-strain relationships that suggest a unified modeling approach. The challenge lies in realizing true torque-stiffness decoupling: in biological antagonistic pairs, each muscle can independently modulate its contribution to net force and joint stiffness, but replicating this in artificial systems requires overcoming significant modeling and control challenges.

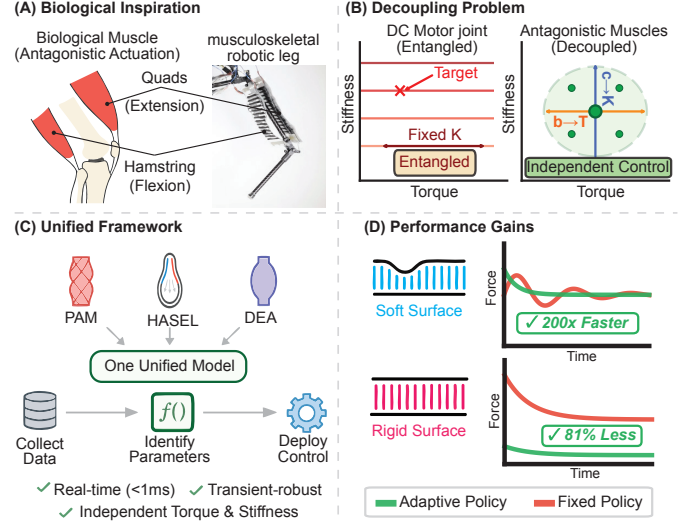


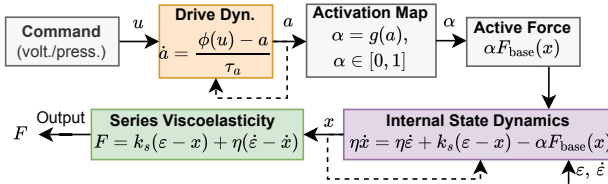
Fig. 1: **(A)** Biological Inspiration: Antagonistic muscle pairs (e.g., quads-hamstring) achieve independent torque-stiffness control through co-contraction and bias. We replicate this principle in musculoskeletal robotic systems using artificial muscles. **(B)** Decoupling Problem: DC motor joints suffer from entangled torque-stiffness control (stiffness is merely a software gain, left), while antagonistic artificial muscles offer plant-level decoupling through dual independent activation channels (α_1, α_2 , right). Using co-contraction/bias coordinates ($c = (\alpha_1 + \alpha_2)/2$, $b = (\alpha_1 - \alpha_2)/2$), we achieve independent control: co-contraction c modulates stiffness K , while bias b generates torque T . **(C)** Unified Framework: Our separable Padé [2/1] force law, experimentally identified from HASEL data, captures PAMs, HASELs, and DEAs in a single model that enables real-time control ($<1\text{ms}$ computation), maintains decoupling through transients, and provides independent torque and stiffness commands. **(D)** Simulation Performance: Adaptive impedance control modulates stiffness according to penetration depth and achieves substantial improvements over fixed-stiffness policies in simulation: 200× faster settling on soft surfaces ($<10\text{ms}$ vs 2.02s) and 81% force reduction on rigid surfaces, demonstrating potential for biological-level robustness across unknown environments.

The core insight from biology is adaptive impedance: muscle stiffness increases with stretch through both intrinsic force-length properties and stretch reflexes, creating a mechanical feedback loop where the penetration depth directly modulates resistance [2], [1]. This principle operates at timescales faster than voluntary control, suggesting it emerges primarily from the physical properties of the muscle-tendon system and low-level

¹Soft Robotics Lab, IRIS, D-MAVT, ETH Zurich, Switzerland {akazemi, rkk}@ethz.ch

* Corresponding author: rkk@ethz.ch

(A) Single Muscle Model



(B) Cascaded Control Architecture

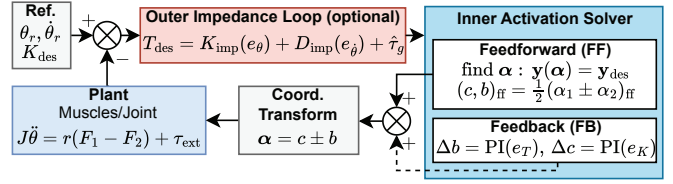


Fig. 2: (A) Single Muscle Model: Command u flows through drive dynamics $\dot{a} = (\phi(u) - a)/\tau_a$ with feedback (dashed), then activation mapping $\alpha = g(a)$ to produce active force $\alpha F_{\text{base}}(x)$. The viscoelastic series branch $[k_s, \eta]$ couples external strain ε to internal deformation x via $\eta \dot{x} = \eta \dot{\varepsilon} + k_s(\varepsilon - x) - \alpha F_{\text{base}}(x)$, with internal feedback (dashed). Output force is $F = k_s(\varepsilon - x) + \eta(\dot{\varepsilon} - \dot{x})$. Two-state dynamics (a, x) capture bandwidth and viscoelasticity; separable Padé law $F_{\text{base}}(x)$ is universal across PAMs, HASELs, DEAs. (B) Cascaded Control Architecture: Optional outer impedance loop generates $T_{\text{des}} = K_{\text{imp}}(e_\theta) + D_{\text{imp}}(e_{\dot{\theta}}) + \hat{\tau}_g$ from position errors for trajectory tracking tasks. Inner activation solver combines feedforward (FF) Newton inverse $\mathbf{y}(\alpha) = \mathbf{y}_{\text{des}}$ with optional feedback (FB) PI controllers $\Delta b = \text{PI}(e_T)$, $\Delta c = \text{PI}(e_K)$ operating in co-contraction/bias (c, b) coordinates. Coordinate transform $\alpha = c \pm b$ combines FF and FB. Plant executes muscle model ($\times 2$) and joint dynamics $J\ddot{\theta} = r(F_1 - F_2) + \tau_{\text{ext}}$. Dashed lines show feedback paths. Outer loop can be bypassed to directly specify $(T_{\text{des}}, K_{\text{des}})$, demonstrating plant-level decoupling independent of any policy-level coupling from impedance control.

reflexes. When contacting soft surfaces, large initial penetration elicits increased stiffness, preventing excessive sinking. On rigid surfaces, minimal penetration maintains low stiffness for shock absorption. This mechanical intelligence (control emerging from physics rather than computation) enables robust interaction without environment classification or explicit force sensing [4], [3].

Conventional robotic actuators cannot replicate this biological capability. In electromagnetic motor-driven joints, stiffness exists only as a software control gain that defines how torque responds to position errors—there is no mechanism to independently command both torque and stiffness at the same instant. Variable stiffness actuators (VSAs) [11], [12] and variable impedance actuators (VIAs) [13], [14] can achieve plant-level torque-stiffness decoupling through dedicated mechanical mechanisms (separate actuators, clutches, or transmissions for independent stiffness adjustment) but at the cost of added weight, complexity, and reduced backdrivability. Antagonistic artificial muscles offer an inherently simpler alternative: *two independent control channels* (α_1, α_2) provide plant-level decoupling through co-contraction (stiffness) and bias (torque) without additional hardware [15], [16]. Yet realizing this decoupling remains challenging: during contact transitions (precisely when impedance modulation matters most), existing controllers lose torque-stiffness independence, causing oscillations on soft surfaces and excessive forces on rigid ones. Without real-time capable models that maintain decoupling through transients, safe interaction with unknown environments remains difficult to achieve.

Prior control approaches using antagonistic actuation have demonstrated independent stiffness modulation [15], [16], but rely on specialized mechanical designs (quadratic springs, VSA mechanisms) or feedback-intensive methods. For artificial muscles specifically, prior modeling efforts have failed to enable practical torque-stiffness decoupling for three operational reasons. First, quasi-static models [5] capture steady-state force-length curves but cannot predict transient behavior, causing

control instability during the critical first 50ms of contact when impedance adaptation occurs. Second, high-fidelity simulations (pneumatic flow dynamics for PAMs [17], electrohydraulic field equations for HASELs [18], [19], or electrostatic models for DEAs [20]) exceed real-time computational budgets by 10-100 \times , making them unsuitable for control. Third, existing models are actuator-specific and require manual tuning for each muscle configuration, preventing the development of generalizable control strategies. These limitations mean that current antagonistic muscle systems cannot execute the depth-adaptive impedance modulation that makes biological systems so robust: they either oscillate uncontrollably on soft surfaces or generate damaging impact forces on rigid ones.

To address these challenges, we present a unified modeling and control framework that maintains torque-stiffness decoupling through contact transients in soft antagonistic artificial muscles. Our approach combines three key innovations: (1) a separable Padé [2/1] force law (rational function with quadratic numerator and linear denominator) that unifies PAMs, HASELs, and DEAs while preserving their distinct physics through a single parameter, (2) a minimal two-state dynamic wrapper that captures bandwidth limitations and viscoelasticity without sacrificing real-time performance, and (3) a cascaded control architecture with analytical inverse dynamics that maintains impedance targets even during model error. The model is identified from experimental HASEL data and validated in simulation with contact tasks. This framework demonstrates how soft artificial muscles could execute the same adaptive impedance strategies observed in biology. By addressing the transient decoupling problem for soft actuators, this work provides a foundation for soft robots to interact safely and adaptively with unstructured environments without explicit sensing or terrain classification.

The key contributions of this work are:

- 1) **Unified modeling framework:** A separable Padé [2/1] force law that captures PAMs, HASELs, and DEAs

through actuator-specific activation mappings, wrapped in a minimal two-state dynamic model (sub-ms computation) that maintains real-time performance while capturing transient bandwidth and viscoelastic effects.

- 2) **Decoupling control architecture:** A cascaded controller combining feedforward inverse dynamics with lightweight PI feedback that maintains independent torque-stiffness tracking through contact transients and model error, enabling soft artificial muscles to perform dynamic contact and interaction tasks.
- 3) **Bio-inspired interaction validation:** Simulation-based demonstration that adaptive impedance control—mirroring biological muscle stretch reflexes—using a single surface-agnostic policy, with controlled experiments isolating stiffness modulation as the causal mechanism for improved contact performance.

The significance of this work extends beyond technical metrics: by demonstrating how artificial muscles could replicate biological impedance strategies in simulation, we provide a computational foundation and control framework as a necessary step toward soft robots achieving human-like manipulation capabilities and safe physical interaction. Hardware validation will be critical for practical deployment in applications ranging from prosthetics to collaborative robots, where adaptive compliance is essential for both safety and performance.

II. UNIFIED MODELING FRAMEWORK

The proposed modeling framework is actuator-agnostic, applicable to diverse artificial muscle technologies including pneumatic artificial muscles (PAMs/McKibben), electrohydraulic actuators (HASELs), and dielectric elastomers (DEAs). The model is experimentally validated using HASEL actuators with hardware testbed measurements; the mathematical structure is designed to capture the fundamental force-strain relationships common to these actuator families, though hardware validation on PAMs and DEAs remains future work.

A. Separable Padé Base Force Law

We model each muscle with a separable active force

$$F(\alpha, z) = \alpha F_{\text{base}}(z), \quad F_{\text{base}}(z) = \frac{c_0 + c_1 z + c_2 z^2}{1 + d_1 z}, \quad (1)$$

where $\alpha \in [0, 1]$ is the normalized activation and z is the strain argument. The Padé [2/1] form is chosen for its minimal parameterization (4 coefficients) while capturing the essential nonlinear force-length relationship common to artificial muscles: positive force at zero strain ($c_0 > 0$), monotonic decay with contraction ($c_1 < 0$), and curvature allowing both convex and sigmoidal shapes (c_2, d_1). Lower-order forms (e.g., linear) fail to capture strain-dependent stiffness, while higher-order forms overfit and introduce unnecessary complexity for real-time control. with coefficients $\mathbf{c} = (c_0, c_1, c_2, d_1)$. The slope at small strain and unit activation is $k_a = c_1 - c_0 d_1$. To ensure physical validity, we require $F_{\text{base}}(z) \geq 0$ and $1 + d_1 z > 0$

over the operating strain interval. The derivative of the Padé base force law is

$$F'_{\text{base}}(z) = \frac{(c_1 - d_1 c_0) + 2c_2 z + d_1 c_2 z^2}{(1 + d_1 z)^2}, \quad (2)$$

which will be used for stiffness calculations.

This Padé [2/1] formulation universally captures diverse muscle physics:

PAMs/McKibben: From the geometric model [17], the force expands to $F = P \cdot (p_0 + p_1 \varepsilon + p_2 \varepsilon^2)$ after strain conversion. Setting $\alpha = P/P_{\text{max}}$ and $d_1 = 0$ in our framework exactly recovers this quadratic form with $c_i = P_{\text{max}} \cdot p_i$.

HASELs: Maxwell stress yields force that depends nonlinearly on strain [6]. Using $\alpha = (V/V_{\text{max}})^2$, the Padé form with $d_1 \neq 0$ captures the characteristic force roll-off at high strains. The denominator term models electrohydraulic coupling where hydraulic constraints limit deformation.

DEAs: For DEAs, force is approximately linear in strain [20]. With $\alpha = (V/V_{\text{max}})^2$, setting $d_1 = 0$ and $c_2 = 0$ yields $F = \alpha(c_0 + c_1 \varepsilon)$.

The coefficient d_1 elegantly distinguishes actuator complexity: $d_1 = 0$ for polynomial force-strain relations (PAMs, simple DEAs), while $d_1 \neq 0$ captures rational mechanics with force saturation (HASELs with hydraulic limits, DEAs with electrode delamination).

During identification, we impose mild shape constraints for physical plausibility: positivity of F_{base} , monotone with contraction, denominator regularity, and near-zero force at maximal contraction.

B. Minimal Two-State Dynamic Wrapper

Finite input bandwidth and internal viscoelasticity are captured with two actuator-side states. A drive state $a(t)$ filters the user command $u(t)$:

$$\dot{a} = \frac{\phi(u) - a}{\tau_a}, \quad \alpha = g(a), \quad (3)$$

where ϕ maps the command to a drive level and g normalizes it to $[0, 1]$.

A Kelvin-Voigt branch in series with the active element introduces an internal deformation $x(t)$ such that

$$F = k_s(\varepsilon - x) + \eta(\dot{\varepsilon} - \dot{x}), \quad (4)$$

$$\eta \dot{x} = \eta \dot{\varepsilon} + k_s(\varepsilon - x) - \alpha F_{\text{base}}(x). \quad (5)$$

The parameters $k_s \geq 0$ and $\eta \geq 0$ represent series stiffness and damping, respectively. When $\tau_a \rightarrow 0$, $k_s \rightarrow \infty$, and $\eta \rightarrow 0$ the quasi-static force law is recovered.

C. Antagonistic Joint with Gravity

For a revolute joint with moment arm r and reference length L_0 , strain maps as $\varepsilon_i = (-1)^i \xi \theta$ where $\xi = r/L_0$. Joint dynamics with equivalent inertia J_{eq} , passive elements (B_j, K_j), and gravity torque $\tau_g(\theta) = m_\ell g \ell_c \sin(\theta - \theta_g)$ become

$$J_{\text{eq}} \ddot{\theta} + B_j \dot{\theta} + K_j \theta + \tau_g(\theta) = r(F_1 - F_2) + \tau_{\text{ext}}. \quad (6)$$

a) *Slack handling.*: Tendons can only pull ($F_i \geq 0$). To avoid discontinuities from explicit slack modeling, we enforce a minimum preload $F_i \geq F_{\text{pre}}$ via co-contraction, which keeps both tendons taut throughout the workspace while preserving smooth force–deformation relations.

D. Stiffness Derivation

The per-muscle stiffness combines the active element ($k_{\text{act},i} = \alpha_i F'_{\text{base}}(x_i)$ with F'_{base} from Eq. (2)) in series with the Kelvin–Voigt branch. For discrete-time perturbations at interval Δt , the damping contributes an effective stiffness $\eta/\Delta t$, giving series stiffness $K_s = k_s + \eta/\Delta t$. The harmonic combination of active and series elements yields:

$$K_{i,\text{step}} = \frac{k_{\text{act},i} K_s}{k_{\text{act},i} + K_s}. \quad (7)$$

The total joint stiffness sums contributions from both muscles, plus passive and gravity terms:

$$K_{\text{tot,step}} = r\xi(K_{1,\text{step}} + K_{2,\text{step}}) + K_j + K_g(\theta), \quad (8)$$

which serves as the control target in the cascaded architecture. The antagonistic joint admits a natural coordinate transformation for decoupling:

$$c \triangleq \frac{1}{2}(\alpha_1 + \alpha_2), \quad b \triangleq \frac{1}{2}(\alpha_1 - \alpha_2), \quad (9)$$

where co-contraction c modulates joint stiffness while bias b generates net torque, enabling independent control of both quantities.

III. MODEL IDENTIFICATION AND VALIDATION

a) *Experimental model identification.*: We validate the muscle modeling framework using a custom-designed muscle characterization testbed that records force, position, and velocity for commanded voltages to HASEL actuators at 50 Hz. The identification procedure generalizes to any artificial muscle via appropriate activation mappings ($\alpha = P/P_{\text{max}}$ for PAMs, $\alpha = (V/V_{\text{max}})^2$ for HASELs, $\alpha = (E/E_{\text{max}})^2$ for DEAs). The identification exploits time-scale separation: quasi-static force-strain data from slow, high-activation trials fit the Padé base curve (Eq. (1)) under physics constraints (non-negativity, monotonicity, denominator regularity), while the full dynamic dataset identifies series parameters (k_s, η, τ_a) and validates transient response. All identified muscle parameters and simulation joint parameters are provided in Table I.

The model achieves sub-Newton accuracy (test RMSE = 0.78 N, $R^2=0.83$) across voltage levels on real hardware, confirming the separable Padé structure captures force dynamics without actuator-specific tuning. Figure 3 shows experimental validation on a held-out trajectory. This hardware-validated muscle model forms the foundation for the simulation-based control experiments that follow.

A. Simulation Validation

Numerical integration uses 0.5 ms timesteps with parameters from Table I. Figure 4 demonstrates the separation structure: varying co-contraction $c = \frac{1}{2}(\alpha_1 + \alpha_2)$ at fixed bias modulates

TABLE I: Model parameters from experimental identification (muscle) and simulation setup (joint).

Muscle Parameters (Learned)			Joint & Link Parameters		
Param.	Value	Unit	Param.	Value	Unit
c_0	6.804	N	r	0.03	m
c_1	-171.076	N	L_0	0.16	m
c_2	1087.818	N	J_{eq}	0.2	kg m ²
d_1	5.674	–	B_j	1.0	Nm s/rad
k_s	2370.9	N	K_j	1.0	Nm/rad
η	64.98	N s	m_ℓ	1.0	kg
τ_a	0.040	s	ℓ_c	0.1	m
			I_{cm}	0.1	kg m ²
			g	9.81	m/s ²

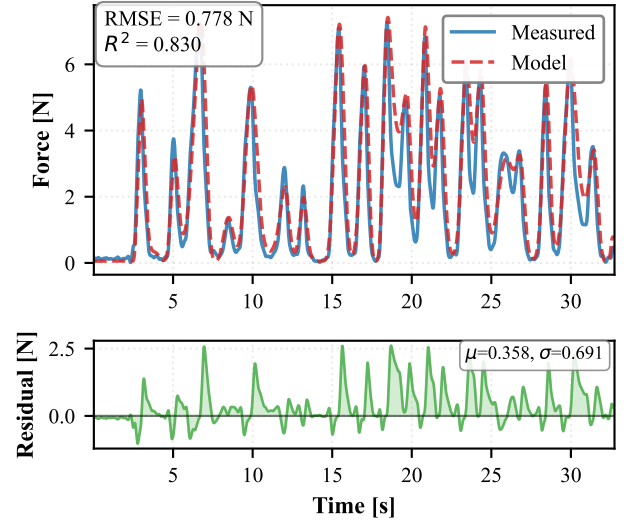


Fig. 3: Experimental validation on held-out test trajectory. Model prediction (red, dashed) tracks measured force (blue) with sub-Newton error (RMSE = 0.78 N, $R^2=0.83$). Residuals remain bounded, validating the separable Padé structure (Eq. (1)) and viscoelastic wrapper (Eqs. (4) and (5)) capture both quasi-static and transient dynamics.

stiffness with negligible torque change (blue, vertical), while varying bias $b = \frac{1}{2}(\alpha_1 - \alpha_2)$ at fixed co-contraction produces torque swings with minimal stiffness variation (orange, horizontal). The gray boundary shows actuation limits. This validates the torque-stiffness decoupling predicted by the stiffness formulation in Eqs. (7) and (8).

IV. MODEL-BASED CONTROL SYNTHESIS

A. Cascaded Architecture

We present a cascaded controller comprising an outer impedance loop and an inner activation solver. The full cascaded system operates as follows:

a) *Outer impedance loop.*: Given position references ($\theta_r, \dot{\theta}_r$) and desired impedance parameters ($K_{\text{imp}}, D_{\text{imp}}$), the outer loop computes the desired torque

$$T_{\text{des}} = K_{\text{imp}}(\theta_r - \theta) + D_{\text{imp}}(\dot{\theta}_r - \dot{\theta}) + \hat{\tau}_g(\theta), \quad (10)$$

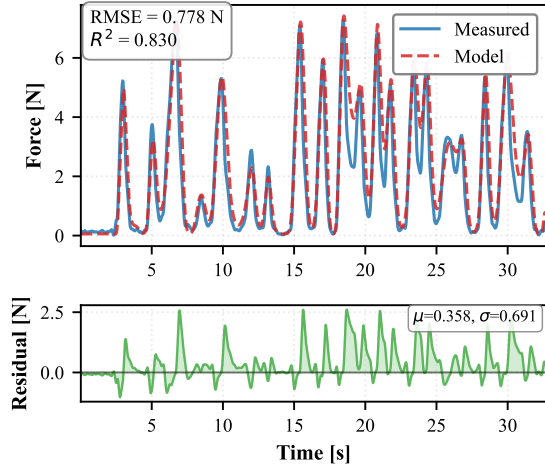


Fig. 4: Torque-stiffness decoupling at $\theta = 0^\circ$. Blue: vary co-contraction c at fixed bias b (stiffness control). Orange: vary bias b at fixed c (torque control). Gray boundary shows feasibility limits. Vertical blue sweeps and horizontal orange sweeps confirm independent control of both quantities.

where $\hat{\tau}_g$ compensates gravity, and K_{imp} , D_{imp} are the impedance gains defining how strongly torque responds to tracking errors. This generates torque commands from position errors for compliant trajectory tracking tasks.

b) Inner activation solver: The inner loop solves for activations $\alpha = [\alpha_1 \ \alpha_2]^\top$ that realize the targets $(T_{\text{des}}, K_{\text{des}})$ while respecting Eqs. (4) and (8). Here K_{des} specifies the desired *mechanical joint stiffness*—a physical property realized through muscle co-contraction—which is conceptually distinct from the outer loop’s impedance gain K_{imp} (though they may be set equal for convenience in trajectory tracking tasks). Importantly, the inner loop can operate independently when $(T_{\text{des}}, K_{\text{des}})$ are directly specified, enabling evaluation of simultaneous torque-stiffness tracking performance without position control. We assemble the muscle torque and active stiffness into

$$\mathbf{y}(\alpha) = \begin{bmatrix} T(\alpha) \\ K_{\text{act,step}}(\alpha) \end{bmatrix} = \begin{bmatrix} r(\alpha_1 F_{\text{base}}(x_1) - \alpha_2 F_{\text{base}}(x_2)) \\ r\xi(K_{1,\text{step}} + K_{2,\text{step}}) \end{bmatrix}, \quad (11)$$

with $K_{i,\text{step}}$ from Eq. (7). The target is $\mathbf{y}_{\text{des}} = [T_{\text{des}}, K_{\text{des}} - K_j - K_g(\theta)]^\top$, so the error is $\mathbf{e}(\alpha) = \mathbf{y}(\alpha) - \mathbf{y}_{\text{des}}$.

c) Operating modes and plant-level decoupling: The cascaded architecture supports two distinct operating modes: (1) **Direct torque-stiffness control**, where $(T_{\text{des}}, K_{\text{des}})$ are externally specified based on task requirements, demonstrating pure plant-level decoupling (Sections IV-D and V); and (2) **Impedance control mode**, where the outer loop generates T_{des} from position errors via Eq. (10), implementing policy-level coupling suitable for compliant trajectory tracking. The contact experiments (Section V) deliberately operate in mode (1), computing T_{des} independently from contact mechanics (preload, gravity, damping) while modulating K_{des} based on penetration depth. This demonstrates that stiffness modulation can occur independently of torque generation, a

plant-level decoupling capability unavailable in DC motor systems where “stiffness” is merely a control gain. While VSA/VIA actuators can also achieve plant-level decoupling, antagonistic muscles provide this inherently through their dual-channel actuation without additional mechanical complexity.

B. Feedforward Open-Loop Controller

The feedforward controller finds activations α^* satisfying $\mathbf{y}(\alpha^*) = \mathbf{y}_{\text{des}}$ via Newton iteration with Jacobian

$$J(\alpha) = \frac{\partial \mathbf{y}}{\partial \alpha} = \begin{bmatrix} \partial T / \partial \alpha_1 & \partial T / \partial \alpha_2 \\ \partial K_{\text{act,step}} / \partial \alpha_1 & \partial K_{\text{act,step}} / \partial \alpha_2 \end{bmatrix}, \quad (12)$$

and update $\Delta \alpha = -(J^\top J + \lambda I)^{-1} J^\top \mathbf{e}$ with regularization $\lambda = 10^{-4}$. The solution converges in 1–2 iterations when warm-started, with final commands $u_i = \Pi_{[0,1]}(\alpha_i + \Delta \alpha_i)$ constrained by saturation and slew limits.

C. Closed-Loop Controller

The closed-loop controller augments feedforward with PI feedback on errors $e_T = T_{\text{des}} - \hat{T}$ and $e_K = K_{\text{des}} - \hat{K}$:

$$\Delta b = K_{pT} e_T + K_{iT} \int e_T dt, \quad \Delta c = K_{pK} e_K + K_{iK} \int e_K dt \quad (13)$$

Combining with feedforward $(c_{\text{ff}}, b_{\text{ff}})$ yields commands $\alpha_i = c_{\text{cmd}} \pm b_{\text{cmd}}$ with anti-windup protection.

PI gains are designed from local plant sensitivities with torque bandwidth 3.0 Hz, stiffness bandwidth 1.0 Hz, and damping ratio $\zeta = 1.2$, ensuring stability while rejecting disturbances.

D. Controller Comparison

Validation tracks orthogonal $(T_{\text{des}}, K_{\text{des}})$ trajectories under disturbances. Figure 5 shows closed-loop control maintains decoupling with $29\times$ lower error than open-loop at 1.0 N m disturbance, achieving sub-ms computation (620 $\mu\text{s}/\text{tick}$) suitable for real-time deployment.

TABLE II: Closed-loop versus open-loop tracking RMSE across disturbance sweep.

Disturbance	RMSE $_T^O$ [N m]	RMSE $_T^C$ [N m]	RMSE $_K^O$ [N m/rad]	RMSE $_K^C$ [N m/rad]
0.5 N m	0.0006	0.0028	0.602	0.832
1.0 N m	0.123	0.0042	0.627	0.832
1.5 N m	0.288	0.097	0.711	0.872

a) Comparison with prior control approaches: While antagonistic muscle systems have been deployed in robotic platforms [8], [9], [10], existing controllers have focused primarily on position tracking rather than independent torque-stiffness control. For example, the HASEL-actuated robotic leg [10] implemented closed-loop position control but did not demonstrate impedance modulation capabilities. Similarly, prior work on PAM-based systems [5] relies on quasi-static models that cannot maintain decoupling through contact transients. Our cascaded architecture uniquely enables real-time independent control of both torque and stiffness during dynamic contact events, as validated through the interaction experiments below.

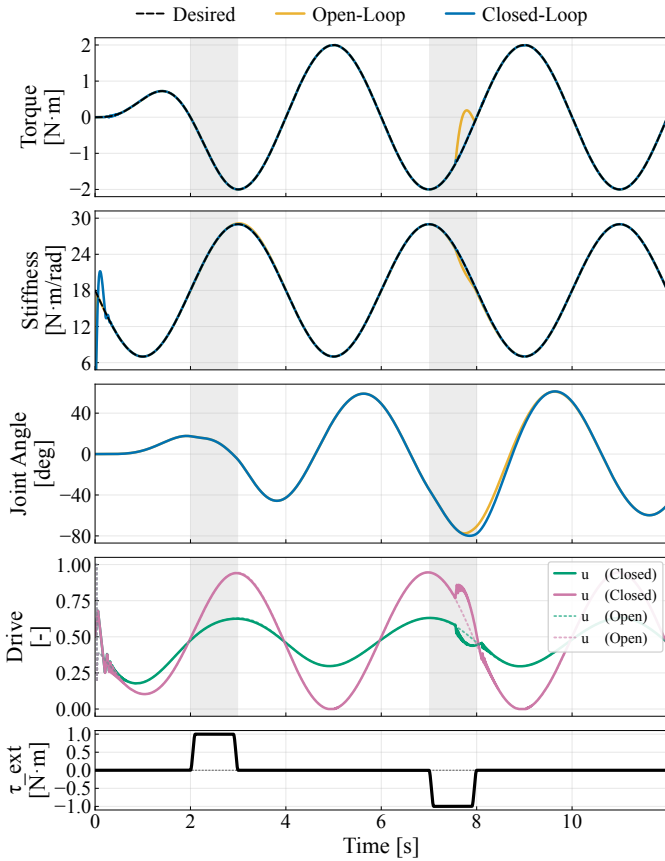


Fig. 5: Controller comparison under ± 1.0 N m disturbances. Open-loop (orange) loses decoupling during disturbances; closed-loop (blue) maintains independent torque-stiffness tracking with $29\times$ lower torque error (Table II). The activation signals show smooth, chatter-free control despite aggressive disturbances. Shading indicates disturbance periods.

V. CONTACT INTERACTION TASKS: VALIDATING BIOLOGICAL STRATEGIES

We demonstrate in simulation that maintained decoupling enables depth-adaptive impedance: stiffness modulation with penetration depth without explicit sensing. Simulation experiments operate in direct torque-stiffness mode: T_{des} from contact mechanics, K_{des} from penetration.

We evaluate three impedance control strategies:

- 1) **Depth-adaptive (bioinspired):** Stiffness modulates based on penetration depth $\delta = \theta - \theta_{\text{contact}}$ via $K_{\text{des}}(\delta) = K_{\text{low}} + (K_{\text{high}} - K_{\text{low}})/(1 + \alpha\delta)$ with $K_{\text{low}} = 6$ N m/rad, $K_{\text{high}} = 20$ N m/rad, $\alpha = 25$ rad $^{-1}$. Torque is computed independently: $T_{\text{des}} = F_{\text{preload}} + \tau_g - B_{\text{eff}}\dot{\theta}$, demonstrating plant-level decoupling.
- 2) **Fixed low:** Constant $K_{\text{des}} = 6.0$ N m/rad throughout contact.
- 3) **Fixed high:** Constant $K_{\text{des}} = 20.0$ N m/rad throughout contact.

Contact is modeled using piecewise linear spring-dampers with $K_{\text{env}} \in \{5$ N m/rad, 500 N m/rad $\}$ representing soft (e.g., foam, sand) and rigid (e.g., wood, metal) surfaces, spanning the

TABLE III: Contact performance metrics. Peak: $\max |\tau_{\text{ext}}|$ in first 20ms. Impulse: $\int |\tau_{\text{ext}}| dt$ during hold (0.3–5s). t_{90} : time to 90% of final. τ_{exp} : exponential decay constant. Stab.: % time in 2% band after 0.5s. θ_{ss} : final position. Bio=Bio-inspired, FL=Fixed-low, FH=Fixed-high.

Surf.	Pol.	Peak [N·m]	Imp. [N·m·s]	t_{90} [s]	τ_{exp} [s]	Stab. [%]	θ_{ss} [rad]
Soft	Bio	3.98	1.05	<0.01	0.39	100	0.25
Soft	FL	4.07	10.55	2.02	1.17	54	0.73
Soft	FH	4.35	14.92	3.49	2.47	22	1.11
Rigid	Bio	11.02	10.48	<0.01	1.09	95	0.20
Rigid	FL	11.28	18.28	<0.01	0.11	100	0.21
Rigid	FH	11.80	54.13	<0.01	0.12	100	0.22

stiffness range encountered in typical manipulation tasks. While this simplified contact model enables controlled comparison of control strategies, future hardware validation will require more sophisticated contact modeling and real-world surface characterization. Contact occurs at $\theta_{\text{contact}} = 0.20$ rad with approach velocity $\dot{\theta}_0 = 4.0$ rad/s. Environment damping $D_{\text{env}} = 0.5$ N m s/rad provides realistic energy dissipation. Each trial runs for 5 s with 1 ms timestep. All strategies use identical policy-level damping ($D_{\text{imp}} = 3.0$ N m s/rad) to ensure fair comparison and isolate stiffness modulation as the causal mechanism.

A. Results

We evaluate performance through settling time t_{90} (time to reach 90% of final position), stability (% time in 2% tolerance band after 0.5 s), peak impact torque $\max_{t \in [0, 20\text{ms}]} |\tau_{\text{ext}}(t)|$, and hold impulse $\int_{0.3}^T |\tau_{\text{ext}}(t)| dt$ (cumulative force during steady contact). Figure 6 and Table III show results.

a) *Soft surfaces* ($K_{\text{env}}=5$ N m/rad):: Fixed-stiffness controllers oscillate uncontrollably (22–54% stability). Depth-adaptive achieves 100% stability with $200\times$ faster settling (<10 ms vs 2.02 s), demonstrating substantial performance improvement by modulating from 6 N m/rad (prevents impact) to 13 N m/rad (provides stability).

b) *Rigid surfaces* ($K_{\text{env}}=500$ N m/rad):: Fixed-high generates excessive forces (54.13 N m s). Depth-adaptive maintains low stiffness at minimal penetration, reducing forces by 81% (10.48 N m s), addressing safety concerns for human interaction.

c) *Biological validation:* Simulation results support the mechanical intelligence principle: effective contact control emerges from depth-impedance coupling, not explicit sensing [1], [2]. This mirrors biological motor control where muscle stiffness increases with stretch through intrinsic force-length properties. The $200\times$ improvement in simulation confirms penetration depth as a natural control signal: large penetration on soft surfaces triggers higher stiffness preventing excessive sinking, while minimal penetration on rigid surfaces maintains compliance. Identical damping across policies isolates stiffness modulation as the causal mechanism. Hardware experiments will be essential to validate these findings under real contact dynamics and actuator limitations.

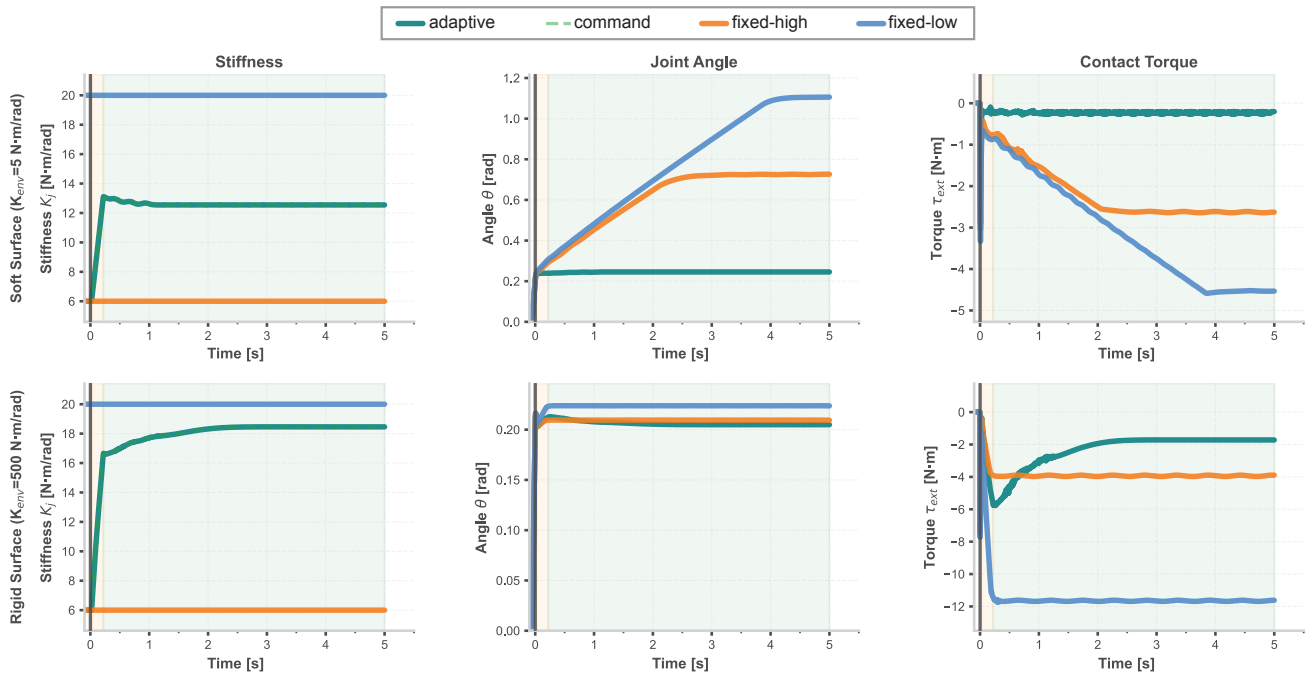


Fig. 6: Simulation results: Depth-adaptive impedance control (teal) modulates stiffness from 6 N m/rad to 13 N m/rad to 18 N m/rad based on penetration depth, achieving 200× faster settling on soft surfaces (top) and 81% force reduction on rigid surfaces (bottom) compared to fixed-low (orange) and fixed-high (blue) policies. Contact modeled as linear spring-dampers. Identical damping ($D_{\text{imp}} = 3.0 \text{ N m s/rad}$) ensures fair comparison.

VI. CONCLUSION

We presented a unified framework for antagonistic artificial muscles that demonstrates adaptive impedance control by modulating stiffness based on penetration depth. Contributions include: (1) a separable Padé [2/1] force law unifying PAMs, HASELs, and DEAs; (2) torque-stiffness decoupling via co-contraction/bias coordinates; (3) a cascaded controller with sub-millisecond computation; and (4) experimental model identification achieving sub-Newton accuracy on HASEL actuators.

Simulation-based contact experiments show 200× faster settling and stable contact on soft surfaces versus 22–54% stability for fixed policies, and 81% force reduction on rigid surfaces. The framework addresses the transient decoupling problem causing oscillations or excessive forces.

a) Limitations and future work: This work presents several important limitations that must be addressed before practical deployment. First, all contact interaction results are simulation-based using simplified linear spring-damper contact models; hardware validation is essential to verify performance under real contact dynamics, actuator nonlinearities, sensing noise, and environmental uncertainty. Second, the model identification currently uses only HASEL actuator data—while the Padé framework is designed to generalize across PAMs and DEAs, experimental validation on these actuator types is needed. Third, the framework assumes symmetric antagonistic muscle pairs with identical parameters; asymmetric configurations and muscle aging effects require further investigation. Fourth,

the cascaded controller requires warm-starting (1–2 Newton iterations) for real-time performance, which may limit rapid transient response. Fifth, we validate only single-DOF systems; multi-DOF extension with coupling effects and computational scaling needs exploration.

Future work priorities include: (1) hardware implementation and experimental validation of the contact strategies on physical HASEL, PAM, and DEA systems; (2) extension to multi-DOF manipulators with workspace-dependent muscle parameters; (3) integration of online parameter adaptation for muscle aging and temperature effects; (4) comparison with learning-based approaches; and (5) validation on real-world manipulation tasks. By providing a computationally validated foundation for how artificial muscles could replicate biological impedance strategies, this work establishes the modeling and control infrastructure necessary as a first step toward making antagonistic muscle systems practically deployable for safe human-robot interaction and adaptive manipulation in unstructured environments.

REFERENCES

- [1] F. E. Zajac, “Muscle and tendon: properties, models, scaling, and application to biomechanics and motor control.” *Critical reviews in biomedical engineering*, vol. 17, no. 4, pp. 359–411, 1989.
- [2] J. C. Houk, “Regulation of stiffness by skeletomotor reflexes,” *Annual review of physiology*, vol. 41, no. 1, pp. 99–114, 1979.
- [3] D. W. Franklin, E. Burdet, K. P. Tee, R. Osu, C.-M. Chew, T. E. Milner, and M. Kawato, “Cns learns stable, accurate, and efficient movements using a simple algorithm,” *Journal of neuroscience*, vol. 28, no. 44, pp. 11 165–11 173, 2008.

- [4] E. Burdet, L. Rey, and A. Codourey, "A trivial and efficient learning method for motion and force control," *Engineering Applications of Artificial Intelligence*, vol. 14, no. 4, pp. 487–496, 2001.
- [5] B. Tondu, "Modelling of the mckibben artificial muscle: A review," *Journal of Intelligent Material Systems and Structures*, vol. 23, no. 3, pp. 225–253, 2012.
- [6] N. Kellaris, V. Gopaluni Venkata, G. M. Smith, S. K. Mitchell, and C. Keplinger, "Peano-hassel actuators: Muscle-mimetic, electrohydraulic transducers that linearly contract on activation," *Science Robotics*, vol. 3, no. 14, p. eaar3276, 2018.
- [7] E. Acome, S. K. Mitchell, T. Morrissey, M. Emmett, C. Benjamin, M. King, M. Radakovitz, and C. Keplinger, "Hydraulically amplified self-healing electrostatic actuators with muscle-like performance," *Science*, vol. 359, no. 6371, pp. 61–65, 2018.
- [8] R. Niiyama, S. Nishikawa, and Y. Kuniyoshi, "Biomechanical approach to open-loop bipedal running with a musculoskeletal athlete robot," *Advanced Robotics*, vol. 26, no. 3-4, pp. 383–398, 2012.
- [9] S. Kurumaya, K. Suzumori, H. Nabae, and S. Wakimoto, "Musculoskeletal lower-limb robot driven by multifilament muscles," *Robomech Journal*, vol. 3, no. 1, p. 18, 2016.
- [10] T. J. Buchner, T. Fukushima, A. Kazemipour, S.-D. Gravert, M. Prairie, P. Romanescu, P. Arm, Y. Zhang, X. Wang, S. L. Zhang *et al.*, "Electrohydraulic musculoskeletal robotic leg for agile, adaptive, yet energy-efficient locomotion," *Nature Communications*, vol. 15, no. 1, p. 7634, 2024.
- [11] B. Vanderborght, A. Albu-Schäffer, A. Bicchi, E. Burdet, D. G. Caldwell, R. Carloni, M. Catalano, O. Eiberger, W. Friedl, G. Ganesh *et al.*, "Variable impedance actuators: A review," *Robotics and autonomous systems*, vol. 61, no. 12, pp. 1601–1614, 2013.
- [12] A. Jafari, N. G. Tsagarakis, and D. G. Caldwell, "Awas-ii: A new actuator with adjustable stiffness based on the novel principle of adaptable pivot point and variable lever ratio," in *2011 IEEE International Conference on Robotics and Automation*. IEEE, 2011, pp. 4638–4643.
- [13] G. Tonietti, R. Schiavi, and A. Bicchi, "Design and control of a variable stiffness actuator for safe and fast physical human/robot interaction," in *Proceedings of the 2005 IEEE international conference on robotics and automation*. IEEE, 2005, pp. 526–531.
- [14] A. Albu-Schaffer, O. Eiberger, M. Grebenstein, S. Haddadin, C. Ott, T. Wimbock, S. Wolf, and G. Hirzinger, "Soft robotics," *IEEE Robotics & Automation Magazine*, vol. 15, no. 3, pp. 20–30, 2008.
- [15] S. A. Migliore, E. A. Brown, and S. P. DeWeerth, "Biologically inspired joint stiffness control," in *Proceedings of the 2005 IEEE international conference on robotics and automation*. IEEE, 2005, pp. 4508–4513.
- [16] I. Sardellitti, G. Palli, N. G. Tsagarakis, and D. G. Caldwell, "Antagonistically actuated compliant joint: Torque and stiffness control," in *2010 IEEE/RSJ International Conference on Intelligent Robots and Systems*. IEEE, 2010, pp. 1909–1914.
- [17] C.-P. Chou and B. Hannaford, "Measurement and modeling of mckibben pneumatic artificial muscles," *IEEE Transactions on robotics and automation*, vol. 12, no. 1, pp. 90–102, 1996.
- [18] Z. Liu, H. McAleese, A. Weightman, and G. Cooper, "Optimization of hydraulically amplified electrostatic actuators based on an evolutionary strategy and finite element model to match the performance of the human triceps surae muscle fibres," *Extreme Mechanics Letters*, vol. 63, p. 102050, 2023.
- [19] S.-D. Gravert, E. Varini, A. Kazemipour, M. Y. Michelis, T. Buchner, R. Hinchet, and R. K. Katzschmann, "Low-voltage electrohydraulic actuators for untethered robotics," *Science Advances*, vol. 10, no. 1, p. eadi9319, 2024.
- [20] M. Wissler and E. Mazza, "Electromechanical coupling in dielectric elastomer actuators," *Sensors and Actuators A: Physical*, vol. 138, no. 2, pp. 384–393, 2007.